INTERFACE

royalsocietypublishing.org/journal/rsif

Research

Cite this article: Pei Z, Chang L, Bai F, Harrison RJ. 2023 Micromagnetic calculation of the magnetite magnetosomal morphology control of magnetism in magnetotactic bacteria. *J. R. Soc. Interface* **20**: 20230297. https://doi.org/10.1098/rsif.2023.0297

Received: 23 May 2023
Accepted: 31 August 2023

Subject Category:
Life Sciences–Earth Science interface

Subject Areas:
biomaterials, computational biology, environmental science

Keywords:
magnetotactic bacteria, magnetite magnetosomes, magnetic properties, crystal morphology, micromagnetic simulation

Author for correspondence:
Liao Chang
e-mail: liao.chang@pku.edu.cn

THE ROYAL SOCIETY PUBLISHING

Micromagnetic calculation of the magnetite magnetosomal morphology control of magnetism in magnetotactic bacteria

Zhaowen Pei[1], Liao Chang[1,2], Fan Bai[1] and Richard J. Harrison[3]

[1]Laboratory of Orogenic Belts and Crustal Evolution, School of Earth and Space Sciences, Peking University, Beijing 100871, People's Republic of China
[2]Laboratory for Marine Geology, Qingdao National Laboratory for Marine Science and Technology, Qingdao 266071, People's Republic of China
[3]Department of Earth Sciences, University of Cambridge, Cambridge, CB2 3EQ, UK

ZP, 0000-0003-4614-0730; LC, 0000-0002-0165-1310

Magnetotactic bacteria (MTB), which precisely bio-synthesize magnetosomes of magnetite or greigite nanoparticles, have attracted broad interdisciplinary interests in microbiology, magnetic materials, biotechnology and geobiology. Previous experimental and numerical investigations demonstrate a close link among MTB species, magnetosome crystal habits, and magnetic characteristics, but quantitative constraints are currently lacking. In this study, we build three-dimensional finite-element micromagnetic models of intact magnetosome chains in common MTB species and corresponding collapsed chains. Realistic numerical microstructures were constructed for the three typical biogenic magnetite crystal forms—cuboctahedron, prism and bullet. Our calculations reveal characteristic magnetic properties associated with specific magnetite crystal forms and MTB species. Cuboctahedron and bullet crystals show distinct low coercivity (less than 30 mT) and high coercivity (greater than 50 mT) clusters, respectively. Prismatic crystals have a broad range of hysteresis parameters that are strongly controlled by chain structure. This magnetic property clustering, combined with magnetic unmixing methods and electron microscopy observations, can fingerprint biogenic magnetite components in geological and environmental samples. The passive magnetic orientation efficiency of various magnetosome chains was calculated. Some bullet-shaped magnetosome chains have higher magnetic moments than those with cuboctahedron and prism magnetosomes, which may enable larger MTB cells to overcome viscous resistance for efficient magnetic navigation.

1. Introduction

Magnetotactic bacteria (MTB) can move along geomagnetic field lines to more habitable aquatic environments [1]. This magnetic orientation function in bacteria is facilitated through the synthesis of magnetosomes, which are intracellular organelles composed of chain-arranged magnetic nanoparticles of magnetite (Fe_3O_4) or greigite (Fe_3S_4) enveloped by a lipid membrane [1,2]. The precise production of magnetosome nanoparticles with regular crystal forms and a relatively narrow size range are genetically controlled [1,3]. Interacting magnetic particles arranged in a chain produce a dipole moment approximately parallel to the chain axis, which interacts with the external magnetic field to determine the movement orientation of MTB [1,4]. After MTB death, magnetosome nanoparticles can be preserved as magnetofossils in sediments [5], which can record palaeomagnetic signals [6], palaeoenvironmental information [7–9] and ancient microbial activities [10]. Therefore, MTB provides a model system for studying the interface of biological, physical and geological processes.

So far hundreds of MTB species that synthesize various magnetite crystal morphologies (octahedral, cuboctahedral, elongated prismatic, bullet-shaped and tooth-shaped) have been found [2,11]. Li *et al*. [11] suggest that the species-specific nature of the crystal habit of biogenic magnetite can be used as a proxy for taxonomy to trace ancient microbial and environmental conditions. Additionally, magnetite morphology is also closely related to its magnetic properties [12,13]. Therefore, it is essential to establish the link among MTB species, crystal forms and magnetic properties.

Previous studies investigated experimentally the magnetic properties of common MTB species using laboratory-cultivated or wild-type MTB samples [14–18]. These experimental data provide important constraints on the biomineralization mechanism in MTB, and also contribute to the magnetic detection of magnetofossils in geological materials [14–16,18,19]. However, it is currently challenging to obtain pure enriched samples and systematic samples with controlled morphological parameters for many MTB species. Therefore, it is difficult to determine experimentally the systematic range of magnetic properties of varying magnetosome chains and morphologies. Recent development of micromagnetic methods enables quantitative calculations of the magnetic properties of magnetosome chains with changing morphological parameters [20,21], i.e. particle size, particle spacing, particle elongation and chain structure (straight chain, collapsed chain, and ring-shaped chain) [22–28]. However, the majority of simulation work relies on approximated chain models, while micromagnetic models with realistic chains are scarce, especially for the rarely simulated bullet-shaped magnetosome chains.

In this study, we apply a micromagnetic modelling approach [23] to calculate the magnetic properties of typical magnetite-producing MTB species. We select three typical magnetite crystal forms (cuboctahedron, prism and bullet) of MTB to build micromagnetic models using transmission electron microscopic (TEM) images of intact magnetosome chains and collapsed chains. Micromagnetic calculations are performed to determine the magnetic properties and navigation efficiency of biogenic magnetite synthesized by various MTB species.

2. Micromagnetic methods

Biogenic magnetite has multiple crystal forms: cuboctahedral, octahedral, elongated prismatic, tooth-shaped and bullet-shaped [2,11]. Cuboctahedral and octahedral crystals usually have similar two-dimensional projections. The asymmetric two-dimensional projections of tooth-shaped and bullet-shaped crystals are also similar. Therefore, we simulate the three most typical crystal morphology categories of magnetite magnetosomes: cuboctahedron, prism and bullet [29]. We select two typical MTB species in each crystal morphology category: AMB-1 [11] and MSR-1 [3] for cuboctahedron, SHHR-1 [11] and XJHC-1 [30] for prism, WYHR-1 [31] and a rod MTB [2] for bullet (figure 1).

Microstructure models of realistic intact chains were created based on TEM images of MTB using Trelis 16.3 (figure 1). The information about particle position, size and rotation angle of intact magnetosome chains (table 1) was obtained from TEM images using the computer vision library OpenCV-Python (figure 1*d*) following the approach of Bai *et al*. [23]. Bullet-shaped crystals in chains have variable overlap in the two-dimensional images. Therefore, we approximately segmented the overlapping particles. Moreover, we constructed chain collapse models by randomly distributing magnetosome particles in a cube space with controlled spacing (figure 1). These chain collapse models were used as one possible end-member to investigate the effect of chain deformation on magnetic properties, although other chain collapse modes are possible and may provide a closer match to observed magnetic properties [22]. We modelled a range of bullet-shaped particles with varying size and elongation to investigate the effect of crystal form on magnetic properties. Single crystal models with three crystal forms were built: bullet model-1, bullet model-2 and prism for comparison. The modelled bullet crystals have a flat base and a conical tip: bullet model-1 is created by connecting a cylinder and an elongated hemisphere; bullet model-2 only contains an elongated hemisphere. The prism model is used to compare with bullet particles with the same elongation to explore the influence of particle shape on magnetism. In addition, we built bullet models elongating along the [111] and [100] axes to investigate the effect of magnetocrystalline anisotropy. Magnetocrystalline anisotropy axes of magnetite were rotated according to their orientation.

We use the finite element (FE) micromagnetic simulation software MERRILL (version 1.3.5) to calculate the magnetic properties [21]. MERRILL computes a magnetization distribution that minimizes the total magnetic free energy to determine the stable magnetic domain state [21]. The total magnetic free energy E_{tot}, for the normalized magnetization vector $\boldsymbol{M} = (M_x, M_y, M_z)$, is given by

$$E_{tot} = \int_\Omega \left[\begin{array}{c} A|\nabla \boldsymbol{M}|^2 + K_1(M_x^2M_y^2 + M_x^2M_z^2 + M_y^2M_z^2) \\ - M_s(\boldsymbol{H_z}\cdot\boldsymbol{M}) - \frac{1}{2}M_s(\boldsymbol{H_d}\cdot\boldsymbol{M}) \end{array} \right] \mathrm{d}\Omega, \tag{2.1}$$

where A, K_1 and M_s are the temperature-dependent material parameters for the exchange constant, the cubic magnetocrystalline anisotropy constant and the saturation magnetization, respectively; $\boldsymbol{H_z}$ and $\boldsymbol{H_d}$ are the external Zeeman field and the demagnetizing field, respectively [21,32]. More importantly, MERRILL can simulate magnetic particles with realistic and complex shapes in three dimensions using FE methods [21]. Hysteresis loops and back-field isothermal remanent magnetization (IRM) curves of all magnetosome chain models were calculated for all six types of MTB. First-order reversal curve (FORC) [33] diagrams were calculated for both intact and collapsed chain models of MSR-1, SHHR-1 and WYHR-1. Intact and collapsed models were subjected to external magnetic fields with 50 and 20 random directions, respectively. ParaView 5.5.2 was used to visualize the domain states [34].

3. Modelling results

3.1. Hysteresis loops and back-field curves

Micromagnetic simulation results indicate large changes in the coercivity (B_c), the coercivity of remanence (B_{cr}) and the ratio of saturation remanence to saturation magnetization (M_{rs}/M_s) with variable magnetosome crystal forms and chain structures (figure 2 and table 2). Average B_c and B_{cr} values of the intact chains with cuboctahedron, prism and bullet crystals are presented in table 2. Simulated B_c and B_{cr}

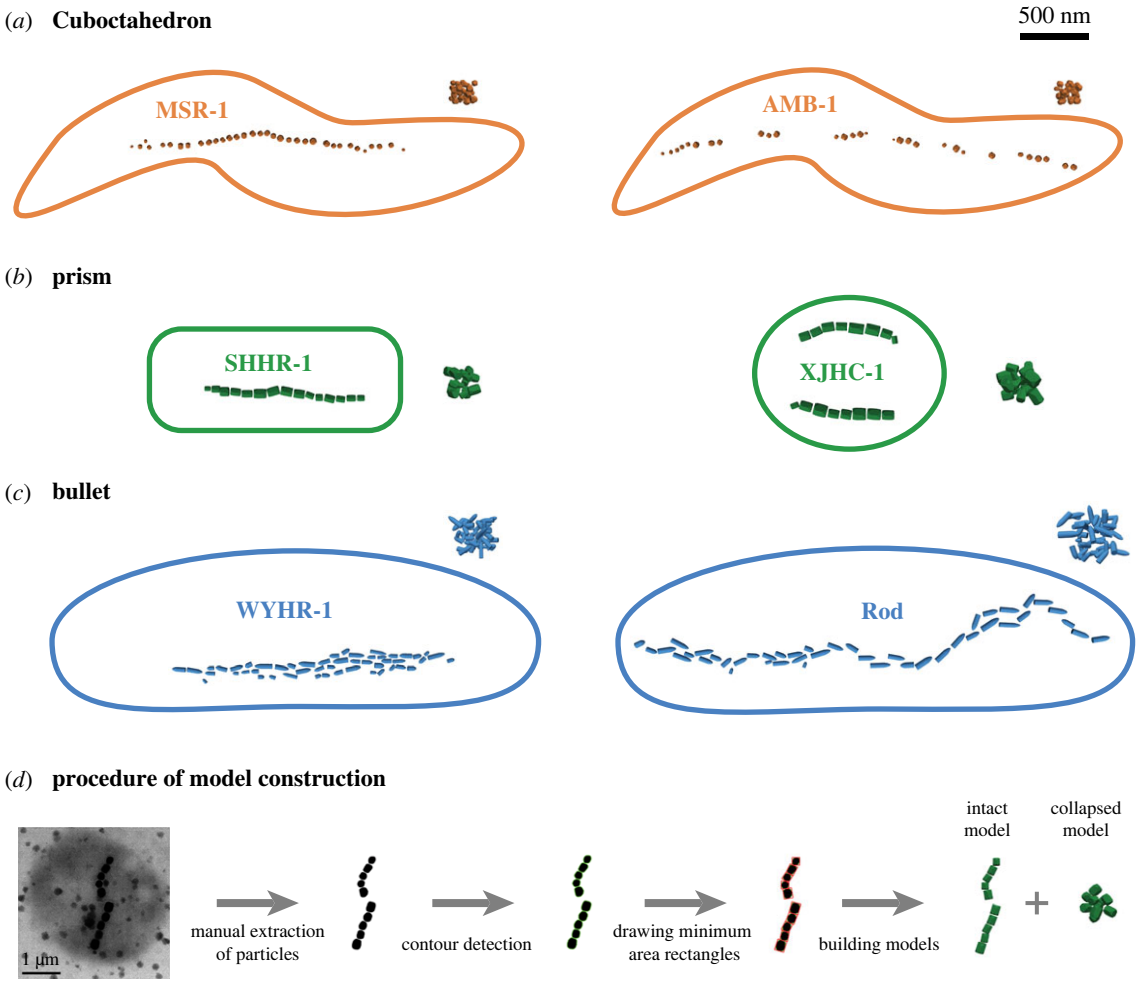

Figure 1. Micromagnetic model constructions of intact biogenic magnetite chains with three crystal forms and the corresponding chain collapse models (*a–c*), and an example of model construction procedures based on microscopic images (*d*). Published transmission electron microscopic (TEM) images of six typical magnetotactic bacteria were used to create these models: (*a*) MSR-1 [3] and AMB-1 [11] for cuboctahedron magnetosomes, (*b*) SHHR-1 [11] and XJHC-1 [30] for prism magnetosomes, (*c*) WYHR-1 [31] and a rod MTB [2] for bullet magnetosomes. Green curves and red rectangles in (*d*) represent detected particle contours and recognized minimum area rectangles using the OpenCV-Python library, respectively.

Table 1. Morphological information of biogenic magnetite from published transmission electron microscopic (TEM) images.

crystal form	MTB type	references	length (nm)	width (nm)	elongation	gap (nm)[a]	particles #
cuboctahedron	MSR-1	Uebe & Schüler [3]	44.54 ± 8.17	41.87 ± 7.53	1.06 ± 0.06	6.08 ± 2.53	34
cuboctahedron	AMB-1	Li *et al.* [11]	47.63 ± 10.99	42.37 ± 10.07	1.13 ± 0.11	7.11 ± 5.31	30
prism	SHHR-1	Li *et al.* [11]	79.11 ± 16.73	58.96 ± 10.54	1.34 ± 0.14	5.06 ± 1.83	15
prism	XJHC-1	Liu *et al.* [30]	100.63 ± 17.20	78.13 ± 15.14	1.30 ± 0.10	3.84 ± 1.86	16
bullet	WYHR-1	Li *et al.* [31]	86.71 ± 29.22	35.69 ± 4.22	2.41 ± 0.72	-	50
bullet	rod	Amor *et al.* [2]	126.78 ± 32.64	42.28 ± 4.89	2.97 ± 0.66	-	44

[a]The particle gap of bullet magnetosome chains cannot be effectively measured owing to irregular chain arrangement and multiple chain branching.

values of intact prism chains and bullet chains are significantly larger than those of intact cuboctahedron chains (figure 2 and table 2). Average M_{rs}/M_s of the intact models is approximately 0.5 (table 2), indicating a dominant uniaxial anisotropy owing to chain arrangement.

Collapsed models of both cuboctahedron and prism magnetosome chains have lower B_c and M_{rs}/M_s than intact chain models (figure 2 and table 2). B_c values of collapsed cuboctahedron models (from 19 to 10 mT for MSR-1 and from 16 to 13 mT for AMB-1, table 2) reduce less than prism models (from 68 to 24 mT for SHHR-1 and from 62 to 15 mT for XJHC-1, table 2). M_{rs}/M_s values of the two cuboctahedron models and XJHC-1 decrease to approximately 0.2–0.3, while this ratio of SHHR-1 only decreases to 0.4 (table 2). B_c values of the collapsed bullet models, however, do not decrease significantly or even increase slightly for some models (from 67 to 53 mT for WYHR-1 and from 79 to 85 mT for a rod MTB, table 2) with constant M_{rs}/M_s of approximately 0.5 (table 2). B_{cr} values of both cuboctahedron and bullet collapsed models are similar to the corresponding intact models

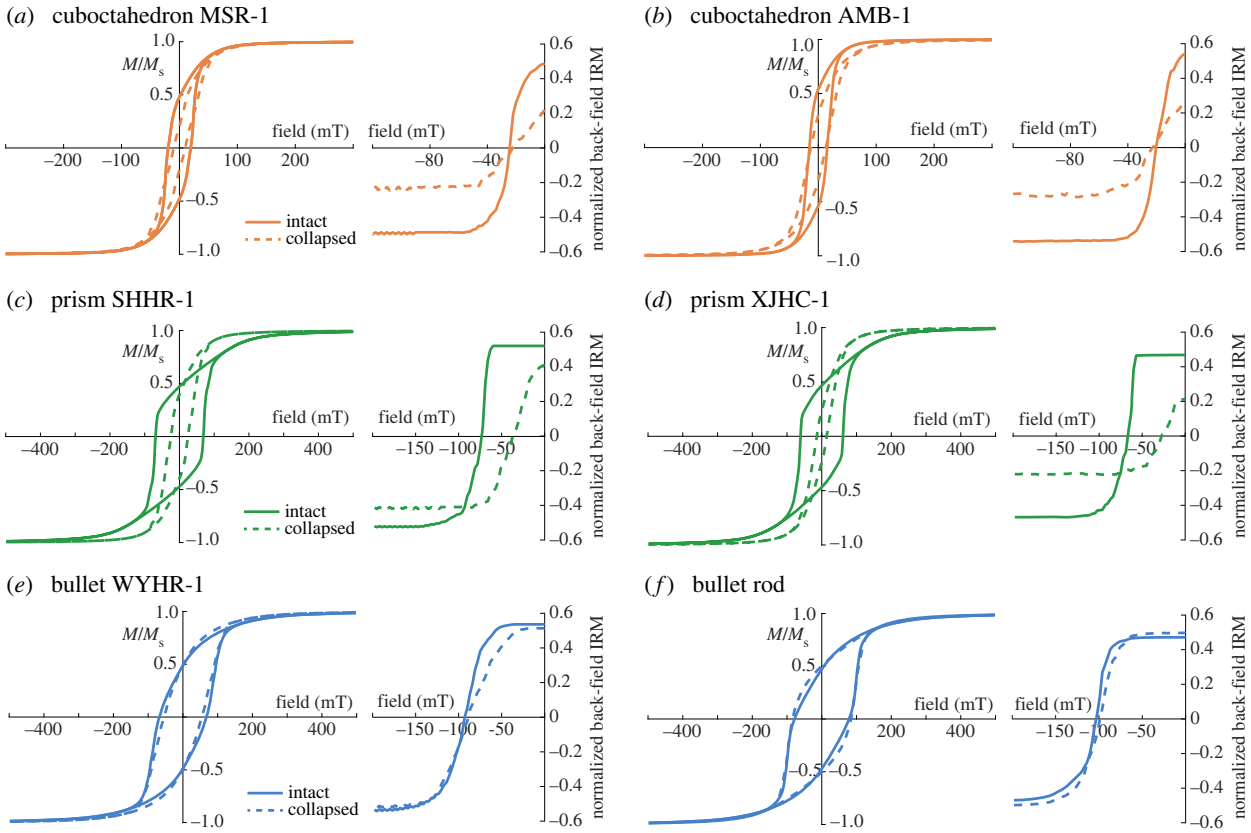

Figure 2. Simulated hysteresis loops and back-field isothermal remanent magnetization (IRM) curves averaged in multiple directions of all intact (solid lines) and collapsed (dashed lines) chain models.

(table 2). Collapsed prism models have significantly reduced B_{cr} compared with intact chain models (from 75 to 39 mT for SHHR-1 and from 66 to 27 mT for XJHC-1, table 2), which indicates that chain collapse has a much stronger influence on the prism magnetosome chains compared with other crystal forms. Decreasing particle spacing reduces the M_{rs}/M_s for both collapsed cuboctahedron and prism models (figure 3*a*, *b*), and reduces the B_c for collapsed prism models (figure 3*b*). However, particle spacing does not obviously affect hysteresis characteristics of bullet models (figure 3*c*).

The switching field distributions calculated from the first derivative of modelled back-field IRM curves for all intact magnetosome chains show an angular dependence. Theoretical predictions using the Stoner–Wohlfarth [38] and the Jacobs–Bean [39,40] models were also calculated. The switching field of cuboctahedron chains is significantly lower than the predicted value (figure 4*a*,*b*), probably owing to the large interparticle distance. Our calculated switching fields are more consistent with prediction from the Jacobs–Bean model (figure 4*a*,*b*). The switching field of the prism and bullet chains agree well with the theoretical predictions from the Jacobs–Bean model (figure 4*c*–*f*).

For the single-particle models, B_c values increase gradually with increasing aspect ratios because of the increase in shape anisotropy (figure 5*a*). Prism model and bullet model-1 (connecting of cylinder and hemisphere) have similar B_c values and are slightly larger than that of bullet model-2 (elongated hemisphere) with aspect ratios greater than 2 (figure 5*a*). This demonstrates that the shape of elongated crystals affects the magnetic properties less than the aspect ratio. Moreover, the B_c values of bullet crystals with the [111] elongation axes are approximately 10–15 mT larger than those of crystals elongating along the [100] direction (figure 5*a*), indicating the significant impact of different easy-axis directions and crystal elongation axis on magnetic properties. The M_{rs}/M_s of all single-particle models are approximately 0.44–0.45 (figure 5*b*).

3.2. Domain states

Magnetite particles in intact chain models are in single-domain states with magnetic moments aligned approximately along the chain direction (figure 6*a*–*f*), indicating a relatively strong magnetostatic interaction between adjacent particles along the chain direction. However, the distorted distribution of magnetic moment directions in collapsed chain models (figure 6*a*–*f*) and the presence of some vortex particles (figure 6*d*) point to magnetic interaction between particles along multiple directions.

3.3. First-order reversal curve diagrams

FORC diagrams of three intact chain models all show a narrow central ridge and a negative lower-left region (figure 7*a*–*c*). Central ridges of the prism (SHHR-1) and bullet models (WYHR-1) are more rightward distributed with higher coercivity than that of the cuboctahedron model (MSR-1, figure 7*a*–*c*). FORC diagrams of three collapsed models manifest the expansion of wings on both sides of the central ridge (figure 7*d*–*f*), indicating relatively strong magnetostatic interactions. The central ridge of the collapsed prism model shifts to the left with reduced coercivity relative to the intact SHHR-1 model (figure 7*b*,*e*). Compared with the intact WYHR-1 model, the central ridge of the collapsed bullet model does not change significantly (figure 7*c*,*f*).

Table 2. Hysteresis parameters and magnetic alignment calculated in this study and experimental data of magnetotactic bacteria and magnetofossils.

crystal form	MTB type	data source	B_c (mT)	B_{cr} (mT)	M_{rs}/M_s	m (10^{-15}Am^2)	m/M_s	$\langle cos\ \theta \rangle$
cuboctahedron	MSR-1	intact model	19	26	0.48	0.46	0.96	0.82
cuboctahedron	MSR-1	collapsed model	10	24	0.22	—	—	—
cuboctahedron	AMB-1	intact model	16	20	0.54	0.46	0.94	0.82
cuboctahedron	AMB-1	collapsed model	13	22	0.30	—	—	—
cuboctahedron	AMB-1	experiment[a]	19	23	0.46	—	—	—
cuboctahedron	AMB-1	experiment[b]	18	23	0.45	—	—	—
cuboctahedron	AMB-1	experiment[c]	31	37	0.50	—	—	—
prism	SHHR-1	intact model	68	75	0.47	1.27	0.97	0.94
prism	SHHR-1	collapsed model	24	39	0.40	—	—	—
prism	XJHC-1	intact model	62	66	0.47	2.96	0.95	0.97
prism	XJHC-1	collapsed model	15	27	0.24	—	—	—
prism	MV-1	experiment[d]	36	44	0.47	—	—	—
bullet	WYHR-1	intact model	67	96	0.49	1.29	0.98	0.94
bullet	WYHR-1	collapsed model	53	90	0.48	—	—	—
bullet	rod	intact model	79	103	0.47	2.13	0.90	0.96
bullet	rod	collapsed model	85	98	0.50	—	—	—
bullet	MYR-1	experiment[e]	55	61	0.59	—	—	—
–	magnetofossil	experiment[f]	20	41	0.24	—	—	—
–	magnetofossil	experiment[f]	19	43	0.22	—	—	—
–	magnetofossil	experiment[f]	19	44	0.22	—	—	—
–	magnetofossil	experiment[g]	23	35	0.40	—	—	—

[a]Li *et al*. [35].
[b]Li *et al*. [36].
[c]Li *et al*. [16].
[d]Jovane *et al*. [14].
[e]Li *et al*. [15]
[f]Chang *et al*. [7].
[g]Ludwig *et al*. [37].

4. Discussion and conclusion

4.1. Linkages between magnetosome crystal morphology and magnetic properties

We plotted simulated hysteresis parameters of intact magnetosome chain models and strong collapse models for different MTB species in the Day diagram (figure 8*a*) [42] and the Néel diagram (figure 8*b*) [43]. Different crystal forms show less obvious clustering in the Day diagram because of the overlapping B_c/B_{cr} (figure 8*a*). In contrast, magnetosome chains with three crystal forms show a clear linkage to their hysteresis parameter ranges in the Néel diagram (figure 8*b*). This demonstrates that the Néel diagram is a better tool for the magnetic identification of magnetosome crystal morphologies. Cuboctahedron magnetosome chains show specific clustering regions in the Néel diagram (figure 8*b*): data for cuboctahedron magnetosome chains have typically low coercivity (less than 30 mT) and move to the lower-left region with decreasing B_c and M_{rs}/M_s during chain collapse. This is mainly owing to the large spacing between cuboctahedron particles in chains, which significantly reduces the coercivity [24,46]. The simulated coercivity of AMB-1 (16 mT) is close to the experimental data of the cultured AMB-1 (18–31 mT) [16,35,36]. Bullet magnetosomes in both intact and collapsed chains show distinct magnetic properties (figure 8*b*): high coercivity (53–85 mT), M_{rs}/M_s of approximately 0.5, and not obviously affected by chain collapse, which is consistent with the measured coercivity (55 mT) of MYR-1 synthesizing bullet-shaped magnetite [15]. This indicates that the magnetic properties of bullet-shaped magnetite are dominated by uniaxial anisotropy owing to their higher elongations (table 1). Simulated hysteresis parameters of prism magnetosome chains have a wide distribution and partially coincide with cuboctahedron and bullet, mostly owing to a more pronounced effect of chain collapse on prism chains (figure 8*b*). The experimental coercivity data of MV-1 (36 mT) [14] is lower than that of the simulated prism magnetosome chains (68 mT for SHHR-1 and 62 mT for XJHC-1), probably because of the larger spacing between the magnetite particles in the MV-1 chain which reduces the coercivity [24]. Moreover, the micromagnetic simulation results of Bai *et al*. [23] indicate a coercivity range of approximately 15–21 mT for greigite magnetosomes, which partially overlaps with the range calculated for the cuboctahedron magnetosome in this study (figure 8*b*).

Previous studies indicate a correlation between the crystal habits of biogenic magnetite or greigite and MTB species owing to a strong genetically controlled biomineralization

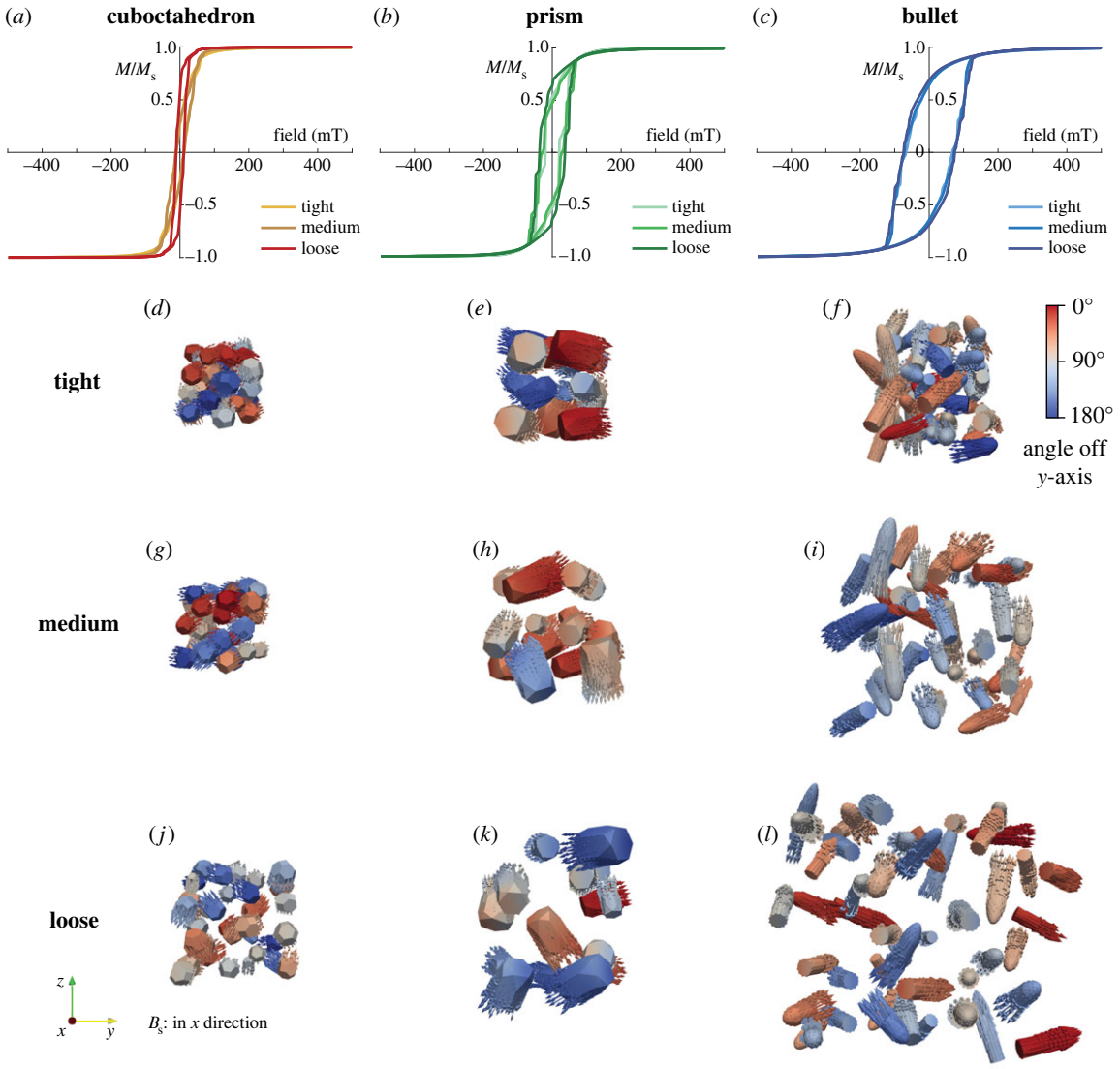

Figure 3. Simulated hysteresis loops and saturation remanent magnetization states of collapsed model for the three types of crystal forms with different spacing (tight, medium and loose). The colour bar represents the angle between the magnetic moment direction and the y-axis. B_s is the applied saturation magnetic field.

[2,11,30,47,48]. For example, *Desulfobacterota* phylum and *Nitrospirota* phylum synthesize straight bullet-shaped and curved bullet-shaped magnetite, respectively [48]. Moreover, MTB have been widely found in various modern aquatic and sedimentary environments [47,49]. In this study, the micromagnetic simulation method based on TEM images can accurately predict the magnetic properties of typical MTB. These magnetic parameters can be used to indicate the crystal morphology of biogenic magnetite, thereby tracing possible MTB species and living environments. However, the correlation among crystal morphology of biogenic magnetite, MTB species and ecology has not been systematically demonstrated owing to the high diversity of MTB species, so a systematic database needs to be established in the future.

4.2. Implications for magnetofossil identification

It is challenging to directly identify *in situ* magnetofossils in sediments or rocks owing to their nanoscale size. Extracting *in situ* magnetofossil information currently relies on rock magnetic techniques, such as principal component analysis of FORC diagrams (FORC-PCA) [50,51] and IRM unmixing [7,8,37,52,53]. Our simulation results demonstrate that the clustering regions in the Néel diagram can be used to distinguish the crystal morphologies of biogenic magnetite (figure 8*b*), and thereby constrain the interpretation of magnetofossil components using magnetic unmixing methods. Furthermore, based on the species specificity of crystal habits of modern MTB discussed in §4.1, this clustering relationship of magnetic signals has the potential to infer possible ancient MTB species of magnetofossils and palaeoecological information.

Previous investigations have identified two typical IRM components of biogenic magnetite in natural samples: lower-coercivity biogenic soft (BS) and higher-coercivity biogenic hard (BH) [52]. BS and BH were considered to represent equant and elongated biogenic magnetite, respectively [52,54–56]. Moreover, recent micromagnetic studies indicate that BH and BS could also be produced by different magnetosome chain structures [25]. Our modelling results provide new constraints for the morphological characteristics of biogenic magnetite indicated by BH and BS: (i) BS represents cuboctahedral biogenic magnetite (both straight and strongly collapsed chains) and prismatic biogenic magnetite with collapsed chain structure; (ii) BH corresponds to all bullet-shaped biogenic magnetite (both straight and strongly collapsed chains), as well as prismatic biogenic magnetite tightly arranged in an approximately straight chain (figure 8*b*). Clearly, BS and BH components originate from

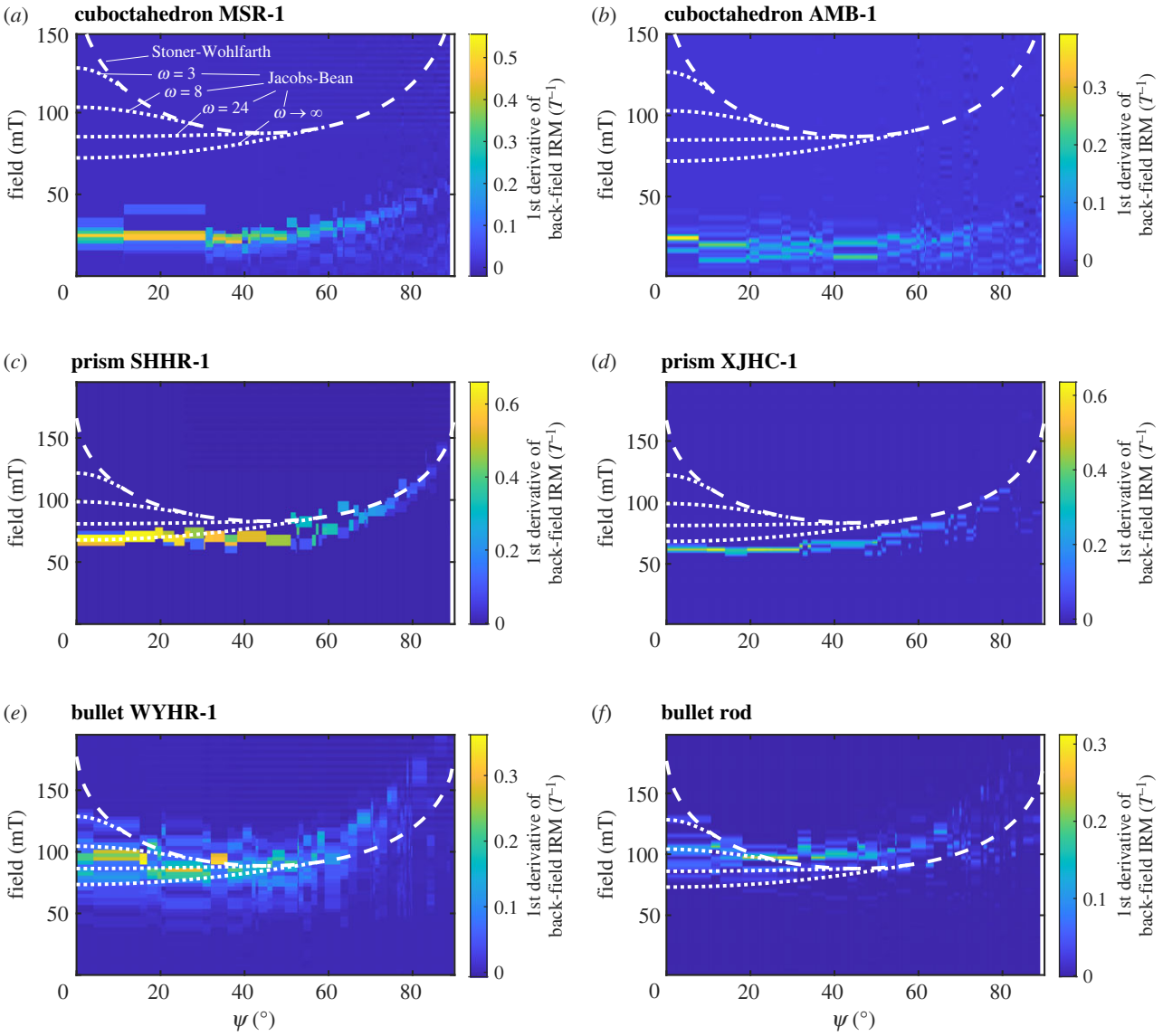

Figure 4. Switching field distribution from the first derivative of back-field isothermal remanent magnetization (IRM) curves for all intact chain models. Ψ is the angle between the applied field and the chain axis. Dashed lines and dotted lines are calculated from the Stoner–Wohlfarth model [38] and the Jacobs–Bean model [39,40] with varying ω (the ratio of saturation magnetization to magnetocrystalline anisotropy field) [40], respectively. Colour bars indicate the first derivative values of normalized back-field IRM for applied magnetic fields.

both biogenic magnetite crystal morphologies and chain structures. Moreover, some of the soft magnetic components may also originate from greigite magnetofossils (figure 8*b*) [23]. Thus, electron microscopy is needed to directly identify biogenic magnetite or greigite in sediments, and the origin of the BH and BS components.

Experimental data of magnetofossils are located in the confidence ellipse of cuboctahedron and prism in the Néel diagram (figure 8*b*), indicating that they are dominant in sediments, while the contributions from bullet-shaped particles or prism particles tightly arranged in linear chains, i.e. represented by BH, are relatively small. Moreover, FORC diagram is also helpful to distinguish the *in situ* chain structure of magnetofossils to determine whether there is possible chain collapse (figure 7) [22,25,26]. For complicated natural samples containing various magnetic minerals, the magnetic approach proposed in this study needs to be combined with other rock magnetic techniques (e.g. FORC-PCA [50,51] and IRM unmixing [52,53]) and microscopic observations to identify magnetic mineral phases.

4.3. Magnetic orientation in magnetotactic bacteria

The magnetic dipole moment of magnetosome chains is used by MTB to orient passively along the external magnetic field [4]. The magnetic energy between the magnetic moment $\boldsymbol{m}$ and the external magnetic field $\boldsymbol{B}$ should exceed thermal energy k_BT (Boltzmann constant k_B multiplied by temperature T) to overcome the rotational Brownian motion. The alignment angle θ between $\boldsymbol{m}$ and $\boldsymbol{B}$ can be evaluated using the Langevin function [57]

$$\langle \cos\theta \rangle = \coth\left(\frac{mB}{k_BT}\right) - \frac{k_BT}{mB}. \tag{4.1}$$

Higher values of $\langle \cos\theta \rangle$ close to 1 indicate a more optimal passive magnetic orientation to the external magnetic field. We calculated the $\langle \cos\theta \rangle$ values for the three modelled MTB using the simulated magnetic dipole moment of magnetosome chains: 0.82 for MSR-1 and AMB-1, 0.94 for SHHR-1 and 0.97 for XJHC-1, and 0.94 for WYHR-1 and 0.96 for a rod MTB (table 2). These results indicate that

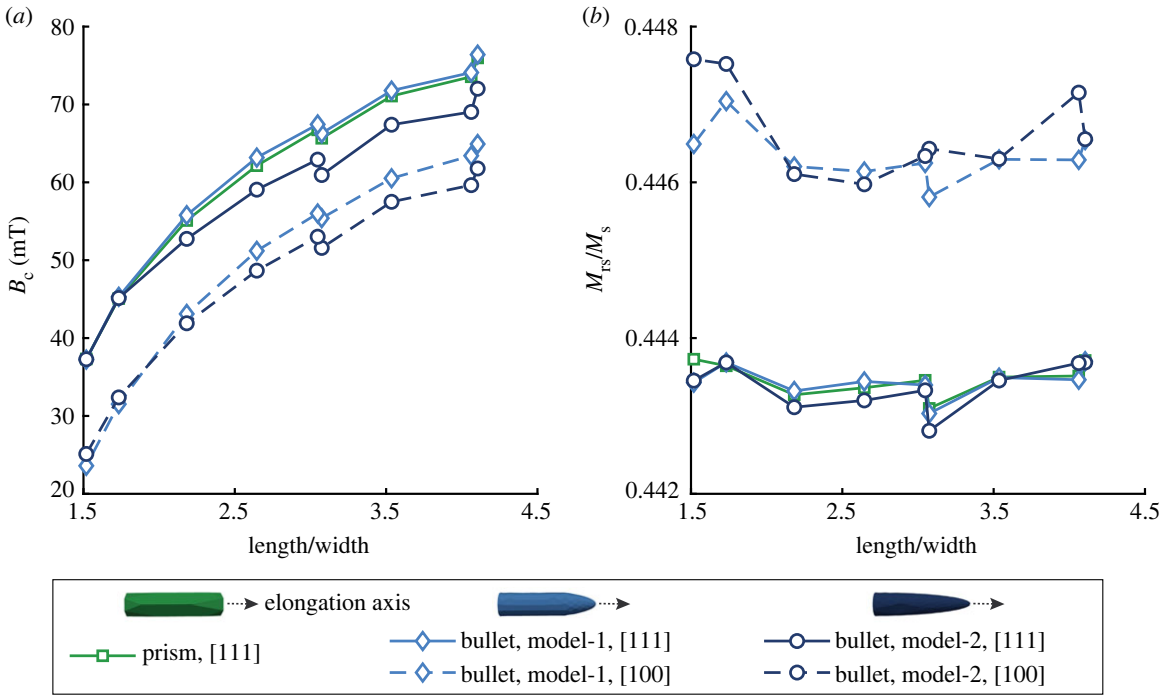

Figure 5. Simulated hysteresis parameters of single-particle models with different aspect ratios: (*a*) coercivity (B_c) and (*b*) the ratio of saturation remanence to saturation magnetization (M_{rs}/M_s). Single-particle bullet models include two geometric forms (bullet model-1 with connecting cylinder and hemisphere; bullet model-2 with elongated hemisphere) and two elongation axes ([111] and [100]).

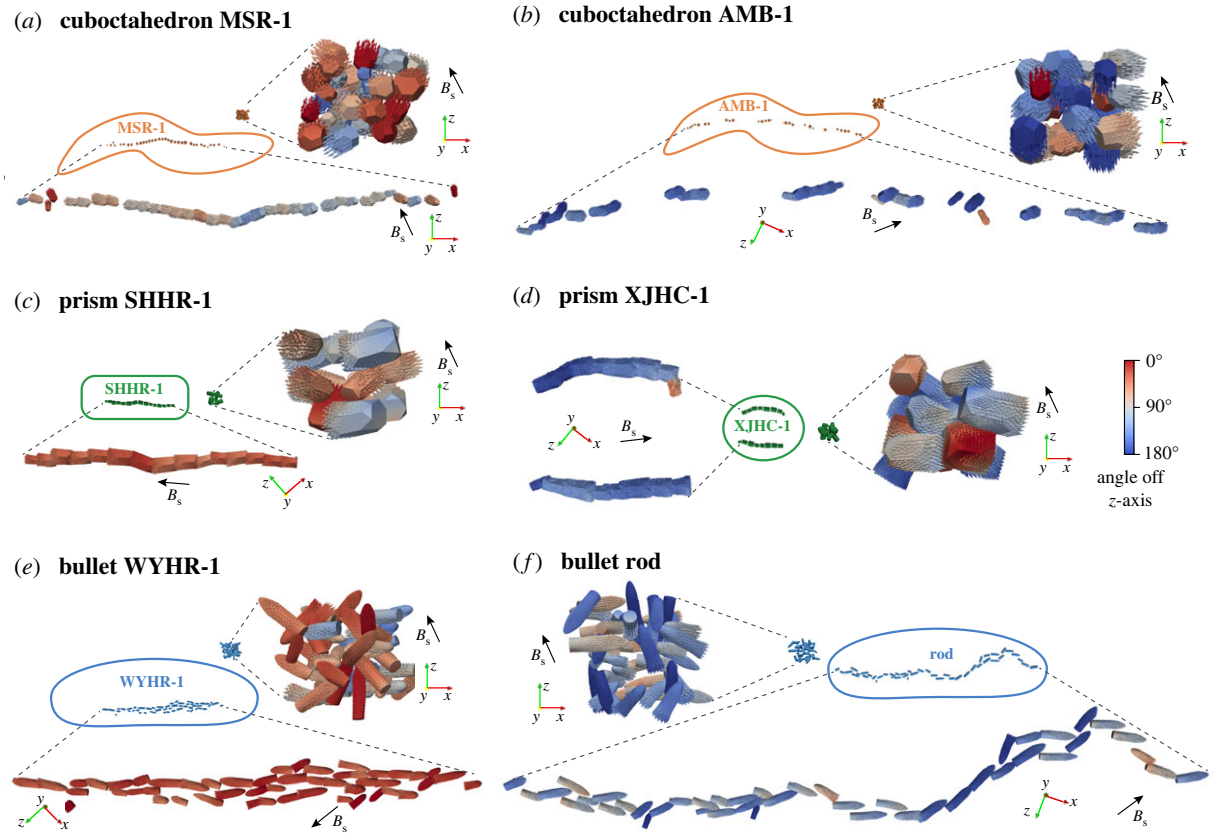

Figure 6. Modelled saturation remanent magnetization states of all intact and collapsed chain models. The black arrow represents the direction of the applied saturation magnetic field. The colour bar represents the angle between the magnetic moment direction and the z-axis. B_s is the applied saturation magnetic field.

MTB with a larger total volume of magnetite in chains has a higher degree of passive orientation.

In contrast to chains containing cuboctahedra and prisms, the chain arrangement of bullet-shaped magnetite is more disordered and the crystal elongation direction is the hard axis [001] rather than the easy axis [111] for some MTB species [11,58]. Our simulation results show that the magnetic properties of bullet-shaped particles are dominated by shape anisotropy (i.e. elongation), as predicted by the previous theoretical model [59]. Thus, bullet magnetosome chains are more

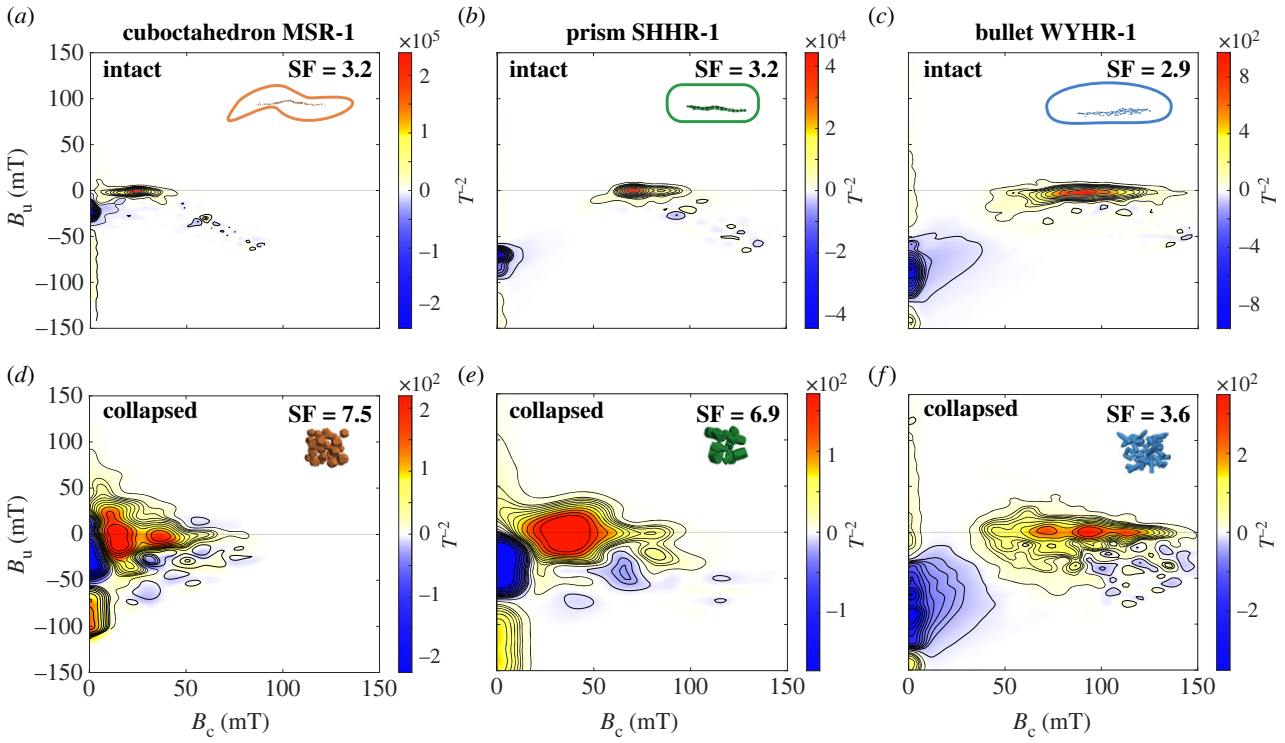

Figure 7. Micromagnetic simulation of first-order reversal curve (FORC) diagrams of intact and collapsed chain models of MSR-1 (*a*,*d*), SHHR-1 (*b*,*e*), and WYHR-1 (*c*,*f*). FORCs were processed using the Forcot software [41]. The smoothing factor (SF) is indicated.

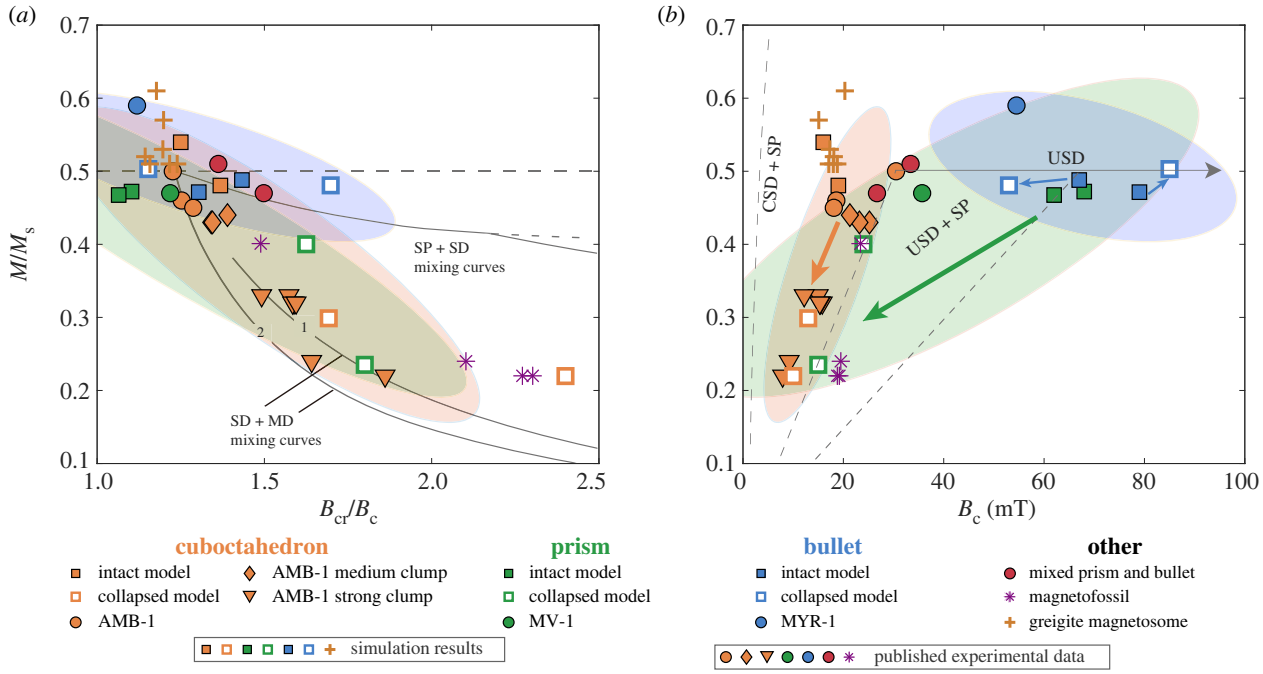

Figure 8. (*a*) Day diagram [42] and (*b*) Néel diagram [43] of simulation results in this study (square) and greigite magnetosomes (cross) [23], and published experimental data of magnetotactic bacteria (circle, diamond, and inverted triangle) and magnetofossils (star) [7,14–16,18,37]. Reference lines in the Day diagram and the Néel diagram are adapted from Dunlop [44] and Tauxe *et al.* [45], respectively. Elliptical regions are the 90% confidence ellipses of all data of each crystal form. Orange, green and blue arrows indicate data trends from intact chain models to collapsed chain models. CSD, cubic single domain; MD, multidomain; SD, single domain; SP, superparamagnetic; USD, uniaxial single domain.

resilient to deviations from perfect chains owing to their high elongations. Simulated bullet and prism magnetosome chains have similar magnetotactic efficiency (approx. 0.95). Therefore, relatively disordered particle arrangement in the chain and elongation along the hard axis do not affect the magnetotactic efficiency of bullet-shaped magnetosomes. Moreover, some large MTB cells, such as giant rod MTB [15,60], produce hundreds of bullet-shaped magnetite crystals with a strong magnetic moment to overcome the viscous resistance [60]. MTB living in sediments need an even larger magnetic moment for magnetic navigation owing to higher viscous drag and poor geomagnetic alignment [61]. Therefore, our simulation results indicate that the bullet-synthesizing MTB can provide a sufficient magnetic moment to adapt to their

larger cell volume and complex living environment, even when the chain deviates from the easy axis and perfect arrangement.

Ethics. This work did not require ethical approval from a human subject or animal welfare committee.

Data accessibility. Relevant data and code are available from the Zenodo repository: https://doi.org/10.5281/zenodo.7960534 [62].

Declaration of AI use. We have not used AI-assisted technologies in creating this article.

Authors' contributions. Z.P.: data curation, formal analysis, investigation, methodology, software, validation, visualization, writing—original draft, writing—review and editing; L.C.: conceptualization, funding acquisition, investigation, resources, supervision, writing—review and editing; F.B.: investigation, methodology, software; R.J.H.: investigation, supervision, writing—review and editing.

All authors gave final approval for publication and agreed to be held accountable for the work performed therein.

Conflict of interest declaration. We declare we have no competing interests.

Funding. This study was supported by a National Natural Science Foundation (NSFC) grant (grant no. 41974074) to L.C., and by a Royal Society-Newton Advanced Fellowship (to L.C. and R.J.H.) jointly funded by the Royal Society (grant no. NAF\R1\201096) and the NSFC (grant no. 42061130214).

Acknowledgements. We thank Editor Tim Holt for efficient editorial handling, and two anonymous referees for providing constructive comments that improved this paper.

References

1. Bazylinski DA, Frankel RB. 2004 Magnetosome formation in prokaryotes. *Nat. Rev. Microbiol.* **2**, 217–230. (doi:10.1038/nrmicro842)
2. Amor M, Mathon FP, Monteil CL, Busigny V, Lefevre CT. 2020 Iron-biomineralizing organelle in magnetotactic bacteria: function, synthesis and preservation in ancient rock samples. *Environ. Microbiol.* **22**, 3611–3632. (doi:10.1111/1462-2920.15098)
3. Uebe R, Schüler D. 2016 Magnetosome biogenesis in magnetotactic bacteria. *Nat. Rev. Microbiol.* **14**, 621–637. (doi:10.1038/nrmicro.2016.99)
4. Klumpp S, Lefèvre CT, Bennet M, Faivre D. 2019 Swimming with magnets: from biological organisms to synthetic devices. *Phys. Rep.* **789**, 1–54. (doi:10.1016/j.physrep.2018.10.007)
5. Kopp RE, Kirschvink JL. 2008 The identification and biogeochemical interpretation of fossil magnetotactic bacteria. *Earth-Sci. Rev.* **86**, 42–61. (doi:10.1016/j.earscirev.2007.08.001)
6. Heslop D, Roberts AP, Chang L, Davies M, Abrajevitch A, De Deckker P. 2013 Quantifying magnetite magnetofossil contributions to sedimentary magnetizations. *Earth Planet. Sci. Lett.* **382**, 58–65. (doi:10.1016/j.epsl.2013.09.011)
7. Chang L, Harrison RJ, Zeng F, Berndt TA, Roberts AP, Heslop D, Zhao X. 2018 Coupled microbial bloom and oxygenation decline recorded by magnetofossils during the Palaeocene–Eocene Thermal Maximum. *Nat. Commun.* **9**, 4007. (doi:10.1038/s41467-018-06472-y)
8. Roberts AP, Florindo F, Villa G, Chang L, Jovane L, Bohaty SM, Larrasoaña JC, Heslop D, Fitz Gerald JD. 2011 Magnetotactic bacterial abundance in pelagic marine environments is limited by organic carbon flux and availability of dissolved iron. *Earth Planet. Sci. Lett.* **310**, 441–452. (doi:10.1016/j.epsl.2011.08.011)
9. Yamazaki T, Kawahata H. 1998 Organic carbon flux controls the morphology of magnetofossils in marine sediments. *Geology* **26**, 1064–1066. (doi:10.1130/0091-7613(1998)026<1064:Ocfctm>2.3.Co;2)
10. Chang SBR, Kirschvink JL. 1989 Magnetofossils, the magnetization of sediments, and the evolution of magnetite biomineralization. *Annu. Rev. Earth Planet. Sci.* **17**, 169–195. (doi:10.1146/annurev.earth.17.1.169)
11. Li J *et al.* 2020 Bullet-shaped magnetite biomineralization within a magnetotactic deltaproteobacterium: implications for magnetofossil identification. *J. Geophys. Res.: Biogeosci.* **125**, e2020JG005680. (doi:10.1029/2020jg005680)
12. Muxworthy AR, Williams W. 2006 Critical single-domain/multidomain grain sizes in noninteracting and interacting elongated magnetite particles: implications for magnetosomes. *J. Geophys. Res.: Solid Earth* **111**, B12S12. (doi:10.1029/2006jb004588)
13. Muxworthy AR, Williams W. 2008 Critical superparamagnetic/single-domain grain sizes in interacting magnetite particles: implications for magnetosome crystals. *J. R. Soc. Interface* **6**, 1207–1212. (doi:10.1098/rsif.2008.0462)
14. Jovane L, Florindo F, Bazylinski DA, Lins U. 2012 Prismatic magnetite magnetosomes from cultivated *Magnetovibrio blakemorei* strain MV-1: a magnetic fingerprint in marine sediments? *Environ. Microbiol. Rep.* **4**, 664–668. (doi:10.1111/1758-2229.12000)
15. Li J *et al.* 2010 Biomineralization, crystallography and magnetic properties of bullet-shaped magnetite magnetosomes in giant rod magnetotactic bacteria. *Earth Planet. Sci. Lett.* **293**, 368–376. (doi:10.1016/j.epsl.2010.03.007)
16. Li J, Wu W, Liu Q, Pan Y. 2012 Magnetic anisotropy, magnetostatic interactions and identification of magnetofossils. *Geochem. Geophys. Geosyst.* **13**, 1–16. (doi:10.1029/2012gc004384)
17. Moskowitz BM, Frankel RB, Bazylinski DA. 1993 Rock magnetic criteria for the detection of biogenic magnetite. *Earth Planet. Sci. Lett.* **120**, 283–300. (doi:10.1016/0012-821x(93)90245-5)
18. Pan Y, Petersen N, Winklhofer M, Davila AF, Liu Q, Frederichs T, Hanzlik M, Zhu R. 2005 Rock magnetic properties of uncultured magnetotactic bacteria. *Earth Planet. Sci. Lett.* **237**, 311–325. (doi:10.1016/j.epsl.2005.06.029)
19. Chang L, Winklhofer M, Roberts AP, Heslop D, Florindo F, Dekkers MJ, Krijgsman W, Kodama K, Yamamoto Y. 2013 Low-temperature magnetic properties of pelagic carbonates: oxidation of biogenic magnetite and identification of magnetosome chains. *J. Geophys. Res.: Solid Earth* **118**, 6049–6065. (doi:10.1002/2013jb010381)
20. Harrison RJ, Lascu I. 2014 FORCulator: a micromagnetic tool for simulating first-order reversal curve diagrams. *Geochem. Geophys. Geosyst.* **15**, 4671–4691. (doi:10.1002/2014gc005582)
21. Ó Conbhuí P , Williams W, Fabian K, Ridley P, Nagy L, Muxworthy AR. 2018 MERRILL: micromagnetic earth related robust interpreted language laboratory. *Geochem. Geophys. Geosyst.* **19**, 1080–1106. (doi:10.1002/2017gc007279)
22. Amor M, Wan J, Egli R, Carlut J, Gatel C, Andersen IM, Snoeck E, Komeili A. 2022 Key signatures of magnetofossils elucidated by mutant magnetotactic bacteria and micromagnetic calculations. *J. Geophys. Res.: Solid Earth* **127**, 1–30. (doi:10.1029/2021jb023239)
23. Bai F, Chang L, Pei Z, Harrison RJ, Winklhofer M. 2022 Magnetic biosignatures of magnetosomal greigite from micromagnetic calculation. *Geophys. Res. Lett.* **49**, e2022GL098437. (doi:10.1029/2022gl098437)
24. Berndt TA, Chang L, Pei Z. 2020 Mind the gap: Towards a biogenic magnetite palaeoenvironmental proxy through an extensive finite-element micromagnetic simulation. *Earth Planet. Sci. Lett.* **532**, 116010. (doi:10.1016/j.epsl.2019.116010)
25. Chang L, Harrison RJ, Berndt TA. 2019 Micromagnetic simulation of magnetofossils with realistic size and shape distributions: linking magnetic proxies with nanoscale observations and implications for magnetofossil identification. *Earth Planet. Sci. Lett.* **527**, 1–12. (doi:10.1016/j.epsl.2019.115790)
26. Pei Z, Berndt TA, Chang L, Bai F, Williams W, Paterson GA. 2022 Bending and collapse: magnetic recording fidelity of magnetofossils from micromagnetic simulation. *J. Geophys. Res.: Solid Earth* **127**, e2021JB023447. (doi:10.1029/2021jb023447)
27. Witt A, Fabian K, Bleil U. 2005 Three-dimensional micromagnetic calculations for naturally shaped magnetite: octahedra and magnetosomes. *Earth Planet. Sci. Lett.* **233**, 311–324. (doi:10.1016/j.epsl.2005.01.043)

28. Zingsem BW, Feggeler T, Terwey A, Ghaisari S, Spoddig D, Faivre D, Meckenstock R, Farle M, Winklhofer M. 2019 Biologically encoded magnonics. *Nat. Commun.* **10**, ARTN 4345. (doi:10.1038/s41467-019-12219-0)
29. Pei Z, Chang L, Xue P, Harrison RJ. 2022 MagNet: automated magnetic mineral grain morphometry using convolutional neural network. *Geophys. Res. Lett.* **49**, e2022GL099118. (doi:10.1029/2022gl099118)
30. Liu P *et al.* 2021 Diverse phylogeny and morphology of magnetite biomineralized by magnetotactic cocci. *Environ. Microbiol.* **23**, 1115–1129. (doi:10.1111/1462-2920.15254)
31. Li J, Zhang H, Liu P, Menguy N, Roberts AP, Chen HT, Wang YZ, Pan Y. 2019 Phylogenetic and structural identification of a novel Magnetotactic *Deltaproteobacteria* strain, WYHR-1, from a freshwater lake. *Appl. Environ. Microbiol.* **85**, 1–11. (doi:10.1128/AEM.00731-19)
32. Nagy L, Williams W, Muxworthy AR, Fabian K, Almeida TP, Ó Conbhuí P, Shcherbakov VP. 2017 Stability of equidimensional pseudo–single-domain magnetite over billion-year timescales. *Proc. Natl Acad. Sci. USA* **114**, 10 356–10 360. (doi:10.1073/pnas.1708344114).
33. Roberts AP, Pike CR, Verosub KL. 2000 First-order reversal curve diagrams: a new tool for characterizing the magnetic properties of natural samples. *J. Geophys. Res.* **105**, 28 461–28 475. (doi:10.1029/2000jb900326)
34. Ahrens J, Geveci B, Law C. 2005 ParaView: an end-user tool for large data visualization. In *Visualization handbook* (eds CD Hansen, CR Johnson), pp. 717–731. Burlington, MA: Elsevier.
35. Li J, Pan Y, Liu Q, Qin H, Deng C, Che R, Yang X. 2009 A comparative study of magnetic properties between whole cells and isolated magnetosomes of *Magnetospirillum magneticum* AMB-1. *Chin. Sci. Bull.* **55**, 38–44. (doi:10.1007/s11434-009-0333-x)
36. Li J, Pan Y, Chen G, Liu Q, Tian L, Lin W. 2009 Magnetite magnetosome and fragmental chain formation of *Magnetospirillum magneticum* AMB-1: transmission electron microscopy and magnetic observations. *Geophys. J. Int.* **177**, 33–42. (doi:10.1111/j.1365-246X.2009.04043.x)
37. Ludwig P, Egli R, Bishop S, Chernenko V, Frederichs T, Rugel G, Merchel S, Orgeira MJ. 2013 Characterization of primary and secondary magnetite in marine sediment by combining chemical and magnetic unmixing techniques. *Global Planet. Change* **110**, 321–339. (doi:10.1016/j.gloplacha.2013.08.018)
38. Stoner EC, Wohlfarth EP. 1948 A mechanism of magnetic hysteresis in heterogeneous alloys. *Philos. Trans. R. Soc. A Math. Phys. Sci.* **240**, 599–642. (doi:10.1098/rsta.1948.0007)
39. Jacobs IS, Bean CP. 1955 Approach to elongated fine-particle magnets. *Phys. Rev.* **100**, 1060–1067. (doi:10.1103/PhysRev.100.1060)
40. Richter HJ. 1996 Analytical formulae of switching fields for fanning in a chain of spheres. *J. Magn. Magn. Mater.* **154**, 263–270. (doi:10.1016/0304-8853(95)00611-7)
41. Berndt TA, Chang L. 2019 Waiting for Forcot: accelerating FORC processing 100× using a fast-Fourier-transform algorithm. *Geochem. Geophys. Geosyst.* **20**, 6223–6233. (doi:10.1029/2019gc008380)
42. Day R, Fuller M, Schmidt VA. 1977 Hysteresis properties of titanomagnetites: grain-size and compositional dependence. *Phys. Earth Planet. In.* **13**, 260–267. (doi:10.1016/0031-9201(77)90108-X)
43. Néel L. 1955 Some theoretical aspects of rock-magnetism. *Adv. Phys.* **4**, 191–243. (doi:10.1080/00018735500101204)
44. Dunlop DJ. 2002 Theory and application of the Day plot (M_{rs}/M_s versus H_{cr}/H_c) 1. Theoretical curves and tests using titanomagnetite data. *J. Geophys. Res.* **107**, EPM-4. (doi:10.1029/2001jb000486)
45. Tauxe L, Bertram HN, Seberino C. 2002 Physical interpretation of hysteresis loops: micromagnetic modeling of fine particle magnetite. *Geochem. Geophys. Geosyst.* **3**, 1–22. (doi:10.1029/2001gc000241)
46. Hanzlik M, Winklhofer M, Petersen N. 2002 Pulsed-field-remanence measurements on individual magnetotactic bacteria. *J. Magn. Magn. Mater.* **248**, 258–267. (doi:10.1016/S0304-8853(02)00353-0)
47. Lefèvre CT, Bazylinski DA. 2013 Ecology, diversity, and evolution of magnetotactic bacteria. *Microbiol. Mol. Biol. Rev.* **77**, 497–526. (doi:10.1128/mmbr.00021-13)
48. Liu P *et al.* 2023 Key gene networks that control magnetosome biomineralization in magnetotactic bacteria. *Natl. Sci. Rev.* **10**, 1–12. (doi:10.1093/nsr/nwac238)
49. Lin W, Pan Y, Bazylinski DA. 2017 Diversity and ecology of and biomineralization by magnetotactic bacteria. *Environ. Microbiol. Rep.* **9**, 345–356. (doi:10.1111/1758-2229.12550)
50. Harrison RJ, Muraszko J, Heslop D, Lascu I, Muxworthy AR, Roberts AP. 2018 An improved algorithm for unmixing first-order reversal curve diagrams using principal component analysis. *Geochem. Geophys. Geosyst.* **19**, 1595–1610. (doi:10.1029/2018gc007511)
51. Lascu I, Harrison RJ, Li Y, Muraszko JR, Channell JET, Piotrowski AM, Hodell DA. 2015 Magnetic unmixing of first-order reversal curve diagrams using principal component analysis. *Geochem. Geophys. Geosyst.* **16**, 2900–2915. (doi:10.1002/2015gc005909)
52. Egli R. 2004 Characterization of individual rock magnetic components by analysis of remanence curves, 1. Unmixing natural sediments. *Stud. Geophys. Geod.* **48**, 391–446. (doi:10.1023/B:SGEG.0000020839.45304.6d)
53. Egli R. 2004 Characterization of individual rock magnetic components by analysis of remanence curves. 3. Bacterial magnetite and natural processes in lakes. *Phys. Chem. Earth* **29**, 869–884. (doi:10.1016/j.pce.2004.03.010)
54. He K, Pan Y. 2020 Magnetofossil abundance and diversity as paleoenvironmental proxies: a case study from southwest Iberian margin sediments. *Geophys. Res. Lett.* **47**, e2020GL087165. (doi:10.1029/2020gl087165)
55. Lascu I, Plank C. 2013 A new dimension to sediment magnetism: charting the spatial variability of magnetic properties across lake basins. *Global Planet. Change* **110**, 340–349. (doi:10.1016/j.gloplacha.2013.03.013)
56. Yamazaki T, Ikehara M. 2012 Origin of magnetic mineral concentration variation in the Southern Ocean. *Paleoceanography* **27**, PA2206. (doi:10.1029/2011pa002271)
57. Frankel RB. 1984 Magnetic guidance of organisms. *Annu. Rev. Biophys. Bioeng.* **13**, 85–103.
58. Li J, Menguy N, Gatel C, Boureau V, Snoeck E, Patriarche G, Leroy E, Pan Y. 2015 Crystal growth of bullet-shaped magnetite in magnetotactic bacteria of the *Nitrospirae* phylum. *J. R. Soc. Interface* **12**, 20141288. (doi:10.1098/rsif.2014.1288)
59. Kornig A, Winklhofer M, Baumgartner J, Gonzalez TP, Fratzl P, Faivre D. 2014 Magnetite crystal orientation in magnetosome chains. *Adv. Funct. Mater.* **24**, 3926–3932. (doi:10.1002/adfm.201303737)
60. Hanzlik M, Winklhofer M, Petersen N. 1996 Spatial arrangement of chains of magnetosomes in magnetotactic bacteria. *Earth Planet. Sci. Lett.* **145**, 125–134. (doi:10.1016/S0012-821x(96)00191-4)
61. Mao X, Egli R, Petersen N, Hanzlik M, Zhao X. 2014 Magnetotaxis and acquisition of detrital remanent magnetization by magnetotactic bacteria in natural sediment: first experimental results and theory. *Geochem. Geophys. Geosyst.* **15**, 255–283. (doi:10.1002/2013gc005034)
62. Pei Z. 2023 Micromagnetic calculation of the magnetite magnetosome in magnetotactic bacteria. Zenodo. (https://doi.org/10.5281/zenodo.7960534)